AgBr/(Sr$_{0.6}$Bi$_{0.305}$)$_2$Bi$_2$O$_7$ Heterostructured Composites: Fabrication, Characterization, and Significantly Enhanced Photocatalytic Activity

Xinling Wang [1] , **Di Zhu** [1], **Yan Zhong** [1,2], **Dianhui Wang** [1,2] **and Chaohao Hu** [1,2,*]

[1] School of Materials Science and Engineering, Guilin University of Electronic Technology, Guilin 541004, China; xlwang04@163.com (X.W.); zhudierzi@163.com (D.Z.); yanzhong@guet.edu.cn (Y.Z.); devix@mails.guet.edu.cn (D.W.)

[2] Guangxi Key Laboratory of Information Materials, Guilin University of Electronic Technology, Guilin 541004, China

[*] Correspondence: chaohao.hu@guet.edu.cn; Tel.: +86-0773-229-1680

check for
updates

Abstract: The pyrochlore-type (Sr$_{0.6}$Bi$_{0.305}$)$_2$Bi$_2$O$_7$ (SBO) containing Bi^{3+} and Bi^{5+} mixed valent states was first investigated as a photocatalyst in our very recent work. To further improve the photocatalytic performance, AgBr/SBO heterostructured composites were synthesized by using a deposition-precipitation method. The characterization of phase structure, morphology, microstructure, elemental composition, and optical properties of the obtained products were performed using X-ray diffractometer (XRD), field emission scanning electron microscopy (FESEM), transmission electron microscopy (TEM)TEM, X-ray photoelectron spectroscopy (XPS), UV-visible diffuse reflectance spectroscopy (UV-vis DRS). The photocatalytic activity of samples was evaluated by degrading methylene blue under visible light illumination. AgBr/SBO composites possess high stability and significantly enhanced photocatalytic performance. The improvement of photocatalytic activity is due to the enhanced light absorption and the separation of photoinduced electrons and holes on the interface of AgBr/SBO heterostructured composites.

Keywords: (Sr$_{0.6}$Bi$_{0.305}$)$_2$Bi$_2$O$_7$; AgBr/(Sr$_{0.6}$Bi$_{0.305}$)$_2$Bi$_2$O$_7$; Heterojunction; Photocatalytic activity

1. Introduction

The rapid development of industry and the increasing consumption of fossil fuels have given rise to the widespread solicitude for the energy shortage and environmental pollution [1–3]. Photocatalysis has been regarded as one of the effective strategies to solve both energy and environment issues, since it can convert solar energy to chemical energy via photochemical reactions and possesses some significant advantages, such as low cost, low temperature depth reaction, simple operation and environmental friendliness [4–6]. Presently, researchers have devoted much effort to exploring various photocatalysts beyond the mostly studied TiO$_2$ [7–10]. Recently, many Bi^{3+}-containing semiconductors like Bi$_2$O$_3$ [11], Bi$_2$WO$_6$ [12], BiVO$_4$ [13], BiOX (X = Cl, Br, I) [14,15], Bi$_2$SnO$_7$ [16], Bi$_2$O$_2$CO$_3$ [17] and some Bi^{5+}-containing oxides like NaBiO$_3$ [18], KBiO$_3$ and MgBi$_2$O$_6$ [19] have drawn considerable attention as new visible light-driven photocatalyst owing to distinctive electronic structure. In particular, Bi$_2$O$_4$ containing Bi^{3+} and Bi^{5+} mixed valent states has been found to exhibit higher photocatalytic degradation efficiency than some widely studied photocatalysts [20].

Among Bi-based oxides, (Sr$_{0.6}$Bi$_{0.305}$)$_2$Bi$_2$O$_7$ (SBO) containing a small amount of vacancies belongs to one kind of special compounds which not only possesses the particular cubic pyrochlore-type crystal structure similar to that of Bi$_2$Sn$_2$O$_7$, but also contains Bi^{3+} and Bi^{5+} mixed valent states. In cubic SBO with space group *Fd*-3*m*, the 16*c* sites (Wyckoff representation) are occupied by Bi^{3+}

and Bi^{5+} ions, and Sr^{2+} and another part of Bi^{3+} ions occupy the 16*d* sites. However, to the best of our knowledge, the detailed physical and chemical properties of SBO are still not studied up to now since the preparation and characterization of SBO have been reported previously by Kumada and co-workers [21]. In our a very recent work [22], considering the structural similarity to cubic $Bi_2Sn_2O_7$ and the coexistence of Bi^{3+} and Bi^{5+} valent states like that in Bi_2O_4, we have successfully synthesized the SBO catalyst and found that SBO is a n-type semiconductor with a band gap (E_g) of 1.25 eV and exhibits high photocatalytic activity and stability under visible light irradiation. However, it must be pointed out that the E_g of SBO is relatively small and the photogenerated charges in it readily recombine with each other. Therefore, it is urgent to enhance the photocatalytic performance of SBO by some modification methods.

Currently, constructing the multicomponent heterostructured composite has been regarded as one of the effective pathways to significantly improve the activity of photocatalysts since it can effectively hinder the recombination of photoinduced carriers [23–26]. AgBr is a p-type semiconductor and has an appropriate E_g of about 2.46 eV [27] and highly photosensitive, and usually used to broaden the range of visible light absorption and further enhance the catalytic activity by constructing the heterojunctions with other semiconductors [28,29]. In particular, our recent studies have also clearly indicated that the photocatalytic properties of the fabricated $AgBr/Bi_2Sn_2O_7$ and $AgBr/MgBi_2O_6$ heterostructured composites are significantly enhanced compared with the corresponding single component [30,31].

In the present work, we first used a facile hydrothermal method to prepare pure SBO catalyst and further fabricated the AgBr/SBO heterostructured composites by using a deposition-precipitation method. The fabricated samples were further characterized by XRD, XPS, SEM, TEM and UV-vis DRS. Under visible light irradiation, the photocatalytic activity of AgBr/SBO composites was investigated by degrading methylene blue (MB) solution. Finally, we discussed detailedly the possible mechanism for enhancing the activity of the composite photocatalysts.

2. Results and Discussion

2.1. Structure and Composition of Catalysts

Figure 1 shows the XRD patterns of pure SBO, AgBr, and AgBr/SBO with variable molar ratio of AgBr to SBO. All patterns of the samples shows sharp diffraction peaks, which means that all samples are well highly crystalline. The diffraction peaks of pure SBO can be well-indexed as the cubic phase of $(Sr_{0.6}Bi_{0.305})_2Bi_2O_7$ (JCPDS No.81-2460). When AgBr/SBO = 1/4, the intensities of XRD peaks of AgBr are relatively weak owing to the low content. With the further increase of AgBr content, the characteristic XRD peaks of AgBr gradually become stronger. When AgBr/SBO = 1/1, the main diffraction peaks of AgBr, such as (200) and (220), have a higher intensity than those of other AgBr/SBO composites. Nevertheless, we must point out that the intensities of characteristic XRD peaks of SBO in AgBr/SBO (4/1) are obviously weaker than those in other composites.
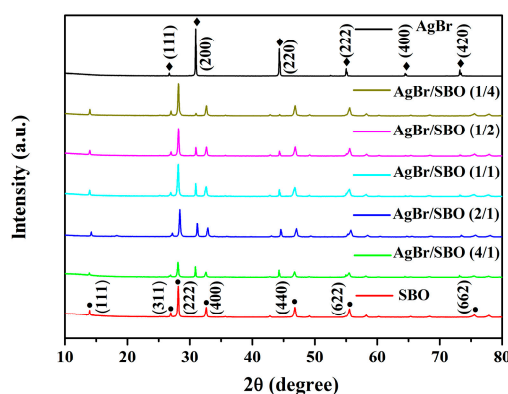

Figure 1. XRD patterns of as-synthesized pure AgBr, SBO, and AgBr/SBO composites.

Figure 2 presents the FTIR spectra of AgBr, SBO, and AgBr/SBO (1/1) composite. Similar prominent peaks at 3450, 1630, and 1382 cm^{-1} are respectively related to the O–H stretching, H–O–H bending, and OH deformation modes due to the adsorbed water molecules [32,33]. The absorption bands around 1475 and 876 cm^{-1} results from the stretching vibration and deformation mode of NO$_3^-$ ions [34,35]. The broad peak located at 606 cm^{-1} belongs to the stretching modes of Bi–O and Sr–O, which are comparable to the Bi–O stretching vibration in the pyrochlore Bi$_2$Sn$_2$O$_7$ [30,36]. The AgBr/BSO (1/1) composite sample shows the characteristic absorption bands of both AgBr and SBO, hereby confirming the coexistence of AgBr and SBO in the fabricated composite sample.
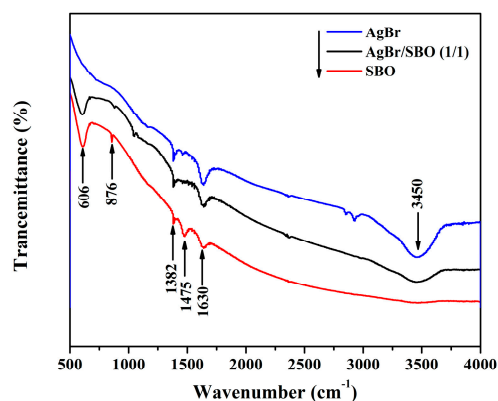

Figure 2. FTIR spectra of AgBr, SBO, and AgBr/SBO (1/1) samples.

The composition and chemical states in AgBr/SBO (1/1) composite are further analyzed by XPS. The full scan spectrum presented in Figure 3a clearly shows that Bi, O, Sr, Ag, and Br elements exist in the as-prepared products and no other elemental signal is detected. The peaks at binding energy of 132.5 and 134.0 eV in Figure 3b correspond to Sr 3d$_{5/2}$ and Sr 3d$_{3/2}$ of Sr^{2+}, respectively. As presented in Figure 3c, the Bi 4f$_{7/2}$ (or Bi 4f$_{5/2}$) peak is split into two bimodal peaks around 158.5 and 159.0 eV (or at 163.6 and 164.2 eV), which are assigned to Bi^{3+} and Bi^{5+} and consistent with the previous report on Bi$_2$O$_4$ [37,38]. The asymmetric O 1s peak for AgBr/SBO (1/1) sample shown in Figure 3d can be splitted into three peaks, which are respectively located at 529.8, 530.7, and 531.1 eV and present three kinds of oxygen species in the AgBr/SBO (1/1) composite. The binding energies around 529.8 eV can be indexed to the lattice oxygen in Sr–O or Bi–O bonds, which is comparable to our previous measurements on Bi$_2$Sn$_2$O$_7$ [30] and MgBi$_2$O$_6$ [31]. The higher binding energies around 530.7 and 531.1 eV correspond to the chemically adsorbed oxygen and physisorbed oxygen, respectively [39]. As shown in Figure 3e, the peaks at 68.3 and 69.3 eV are ascribed to the Br 3d5/2 and Br 3d3/2 of Br$^-$ in AgBr. As presented in Figure 3f, the peaks centered at binding energies of 373.3 and 367.2 eV are respectively ascribed to Ag 3d$_{3/2}$ and Ag 3d$_{5/2}$ of Ag$^+$ in AgBr, which agrees well with our measured values for AgBr/Bi$_2$Sn$_2$O$_7$ and AgBr/MgBi$_2$O$_6$ heterostructured catalysts [30,31].
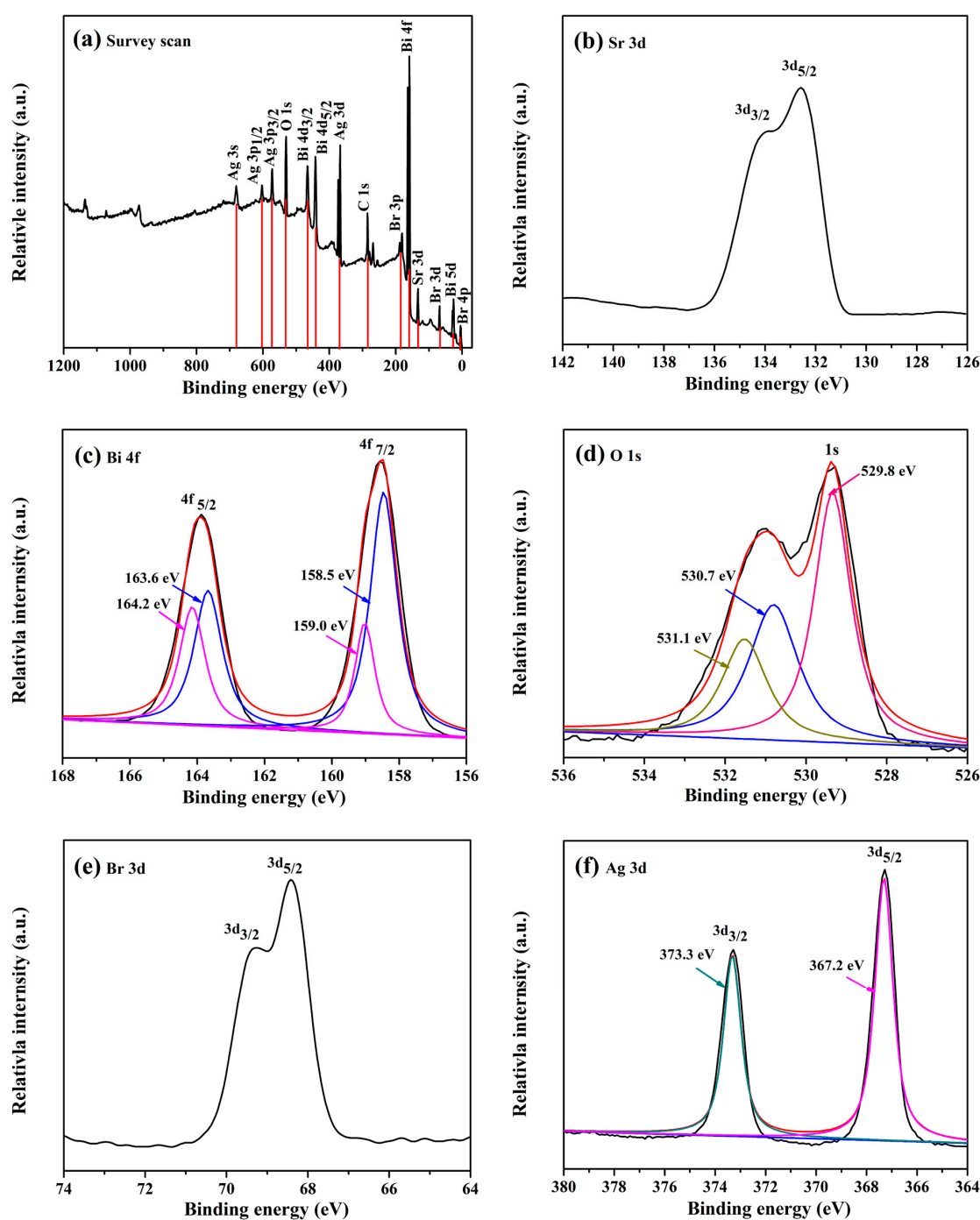
Figure 3. (**a**) typical XPS survey spectra of all elements, and high-revolution spectra of (**b**) Sr 3d, (**c**) Bi 4f, (**d**) O 1s, (**e**) Br 3d, and (**f**) Ag 3d of AgBr/BSO (1/1) composite.

2.2. Morphology Analysis

Figure 4 presents the typical FESEM images of pure SBO, AgBr, and AgBr/SBO (1/1) composite. Pure SBO sample shown in Figure 4a,b is composed of large numbers of irregular blocks with the size from about 0.1 to 0.6 μm. As shown in Figure 4c, the synthesized AgBr product exhibits the smooth and irregular particle-like morphology. The average diameter of the particles is about 1–2 um. Figure 4d presents the FESEM image of AgBr/SBO (1/1) composite. It can be seen that AgBr particles couple well with SBO particles. Moreover, SBO retains the original size and morphology, while the size of AgBr particles in AgBr/SBO (1/1) composite is obviously decreased to about 0.1–0.2 μm. This

means that the prefabricated SBO with relatively rough surface can provide a great deal of nucleation sites for the growth of AgBr particles and finally lead to a uniform dispersion of AgBr particles on it with a smaller size. The EDS elemental mapping of AgBr/SBO (1/1) composite presented in Figure 4e further shows the distribution of AgBr particles on the relatively larger SBO particles.
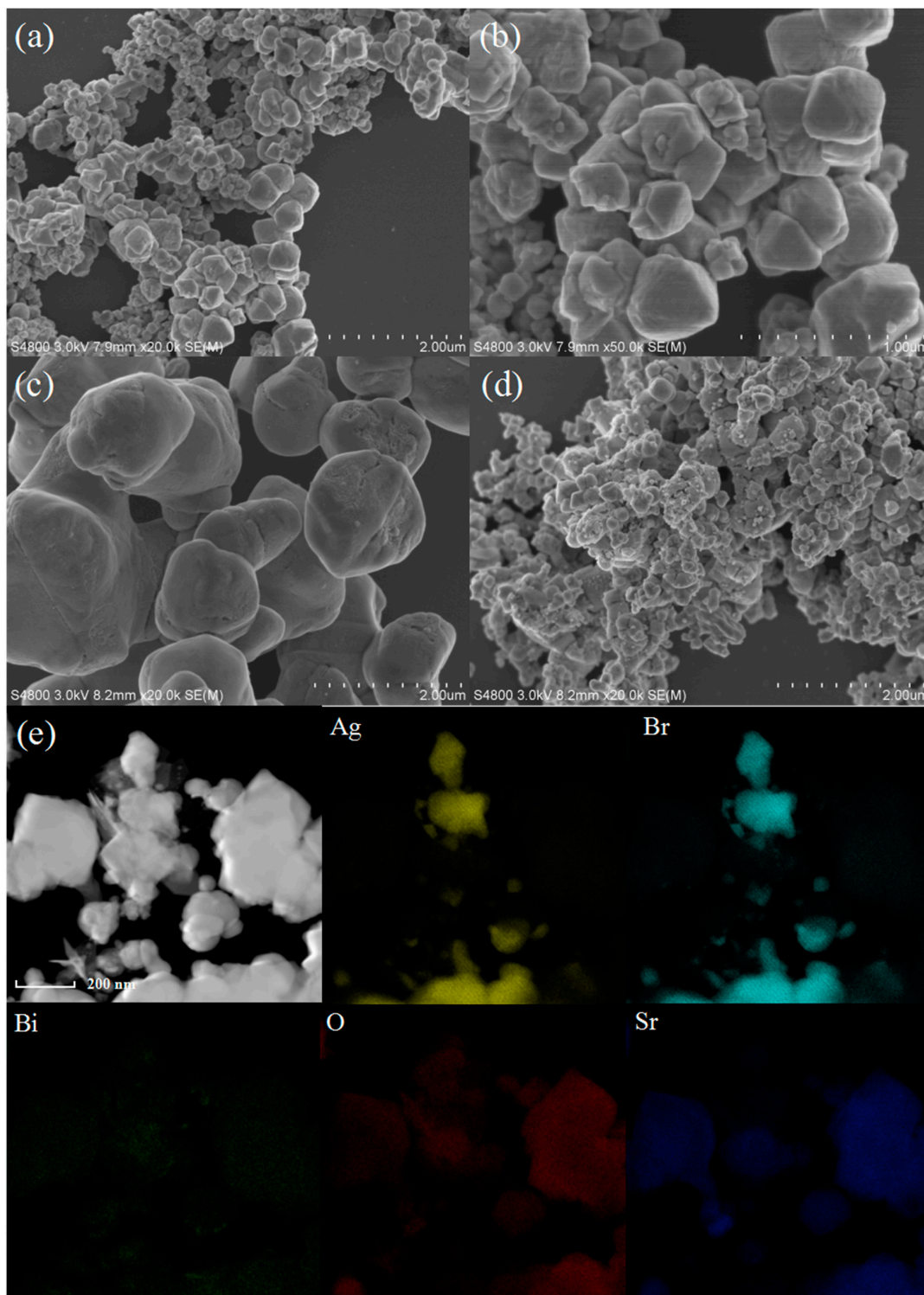

Figure 4. FESEM images of (**a**), (**b**) SBO, (**c**) AgBr, and (**d**) AgBr/SBO (1/1) composite and EDS elemental mapping (**e**) of AgBr/SBO (1/1) composite.

Next, TEM and high resolution TEM (HRTEM) images were used to investigate the detailed microstructural information of AgBr/SBO composites. As clearly shown in Figure 5a, AgBr nanoparticles couple tightly with SBO nanoparticles and the difference in the particle size of two phases is indeed obvious. The two lattice fringe spacings of 0.32 and 0.29 nm observed from the HRTEM presented in Figure 5b correspond to the (222) plane of pyrochlore SBO and the (220) plane of AgBr, respectively. The distinguished interface built between AgBr and SBO clearly shows the formation of AgBr/SBO heterojunction, which is expected to promote the charge separation efficiency in this composite catalyst.
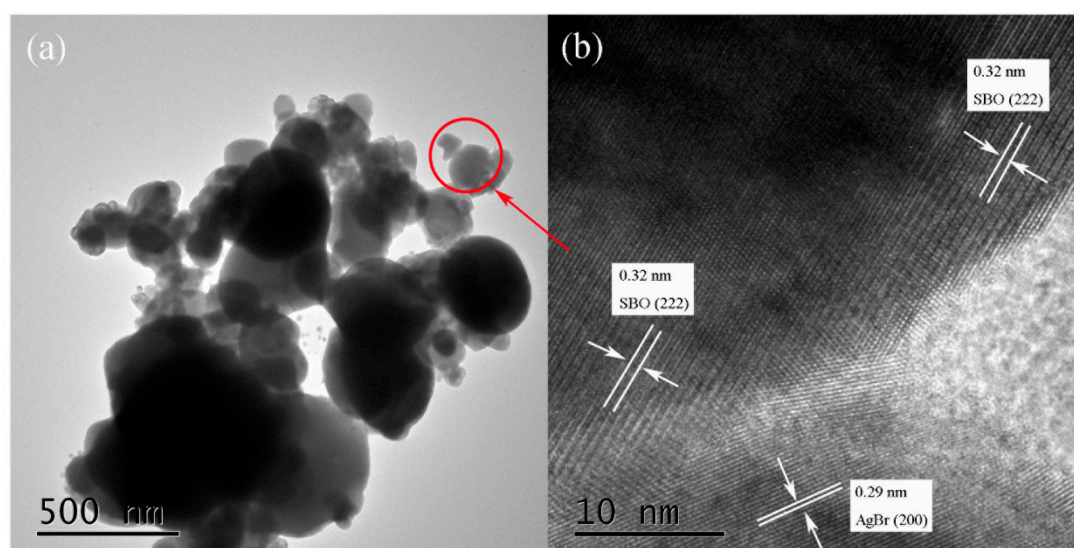

Figure 5. (**a**) TEM and (**b**) HRTEM images of AgBr/SBO (1/1) composite.

2.3. Photophysical Properties of AgBr/SBO Composites

The UV-vis diffuse reflectance spectroscopic investigations on pure AgBr, SBO, and AgBr/SBO composites are presented in Figure 6a. Pure AgBr has a clear absorption band edge around 510 nm. Compared with AgBr, the absorption spectra of pure SBO show a long absorption tail due to its darker hue. The prepared AgBr/SBO catalysts show an increased absorption in the visible light region and the absorbance is gradually enhanced with the increase in the amount of SBO. The E_g can be obtained from the following equation:

$$\alpha h\nu = A(h\nu - E_g)^{n/2} \tag{1}$$

where α, h, ν, and A are the absorption coefficient, Planck's constant, light frequency, and a constant. $n = 1$ is for the direct semiconductor and $n = 4$ is for the indirect semiconductor. For pure SBO and AgBr, n respectively corresponds to 1 and 4 [22,27]. Here, we assume that the prepared AgBr/SBO composite is a direct semiconductor. The E_g of AgBr estimated by the extrapolation of the plot of $(\alpha h\nu)^{1/2}$ versus the energy of a photon ($h\nu$) depicted in Figure 6b is 2.43 eV, being well consistent with the previously reported values [27,30]. The estimated E_g of SBO and AgBr/SBO (1/1) composite are 1.25 and 1.76 eV, respectively.
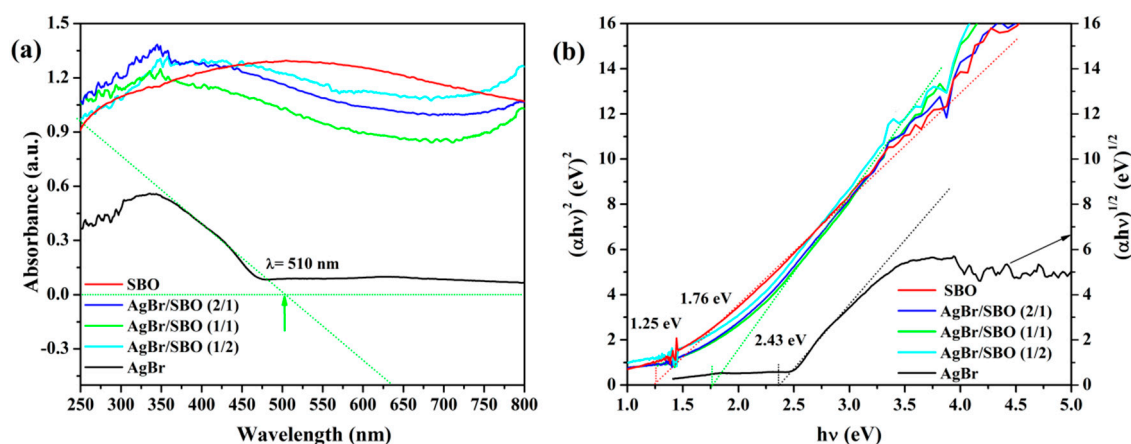
Figure 6. (**a**) UV-vis diffuse reflectance spectra and (**b**) the band gap energy of SBO, AgBr, and AgBr/SBO composites with different molar ratio.

2.4. Photocatalytic Performance of AgBr/SBO Composites

The catalytic activity and chemical stability of AgBr/SBO composites with different molar ratios were evaluated by degrading MB dye solution. As depicted in Figure 7a, the photocatalysis of MB can be negligible without the presence of AgBr, SBO, or AgBr/SBO composites, indicating that the degradation of MB is driven by photocatalysis. Pure SBO shows poor catalytic activity for photodegrading MB solution after 20 min visible light irradiation. AgBr also has no notable effect on MB degradation and only decompose about 40% of MB in 20 min. The measured results presented in Figure 7a indicate that all the as-prepared AgBr/SBO composites show the greatly enhanced photocatalytic activity in comparison with their individual counterpart. In particular, AgBr/SBO (1/1) completely degrades the MB solution within 20 min and shows the best catalytic activity. For comparison, the photocatalytic performance of the physical mixture of AgBr and SBO with the 1/1 molar ratio is measured. It can be found that the activity of AgBr/SBO (1/1) physical mixture is obviously slower than that of as-synthesized AgBr/SBO catalysts. The results clearly show the formation of a heterojunction between SBO and AgBr in the as-prepared AgBr/SBO composites. Under visible light irradiation, in addition, the MB degradation efficiency of AgBr/SBO (1/1) is comparable to that of AgBr/SBO (1/1) only under UV light irradiation, which means that the effect from the visible light excitation on the degradation of MB from is negligible.

The kinetic of MB photodegradation is further discussed. The plots of $\ln(C_0/C)$ versus degradation time presented in Figure 7b are approximately linear, indicating that the degradation of MB over the as-prepared catalysts is first-order. The reaction rate constant of AgBr/SBO (1/1) composite is 0.158 min^{-1}, being about 40 and 45 times larger than those of pure AgBr and SBO, respectively. This clearly shows the excellent efficiency of AgBr/SBO composite catalysts for degrading MB solution. Figure 7c presents the temporal change in the absorption spectra of the dye solution over AgBr/SBO (1/1) composite catalyst. The peak intensity of MB at around 664 nm decreases with increasing photodegradation time, showing the destruction of MB molecular structure mediated by the as-prepared heterostructured catalyst. After 20 min irradiation, the dyes were completely decolorized and no new absorption peaks appeared, which demonstrates that the chromosphere structure of the dyes is completely decomposed.

It is well known that some reactive species including hole (h$^+$), superoxide ($\bullet$O$_2^-$), and hydroxyl ($\bullet$OH) radicals play the key roles in degrading the dye molecules during the photocatalytic oxidation process [40]. Figure 7d shows the MB degradation on AgBr/SBO (1/1) together with some scavengers. Here, the trapping experiments were performed using the 5 mmol of isopropanol (IPA), benzoquinone (BQ), and disodium ethylenediamine tetraacetic acid (EDTA) as the $\bullet$OH, $\bullet$O$_2^-$, and h$^+$ scavenger, respectively [40,41]. As clearly shown in Figure 7d, the degradation efficiency is significantly inhibited using EDTA and IPA scavengers, indicating that the photoinduced h$^+$ and $\bullet$OH are the major active species and serve as a dominated role during the MB degradation on AgBr/SBO catalysts. While the

photodegradation of MB is almost unaffected by adding BQ scavenger, indicating that •O_2^- is the minor active oxygen species.

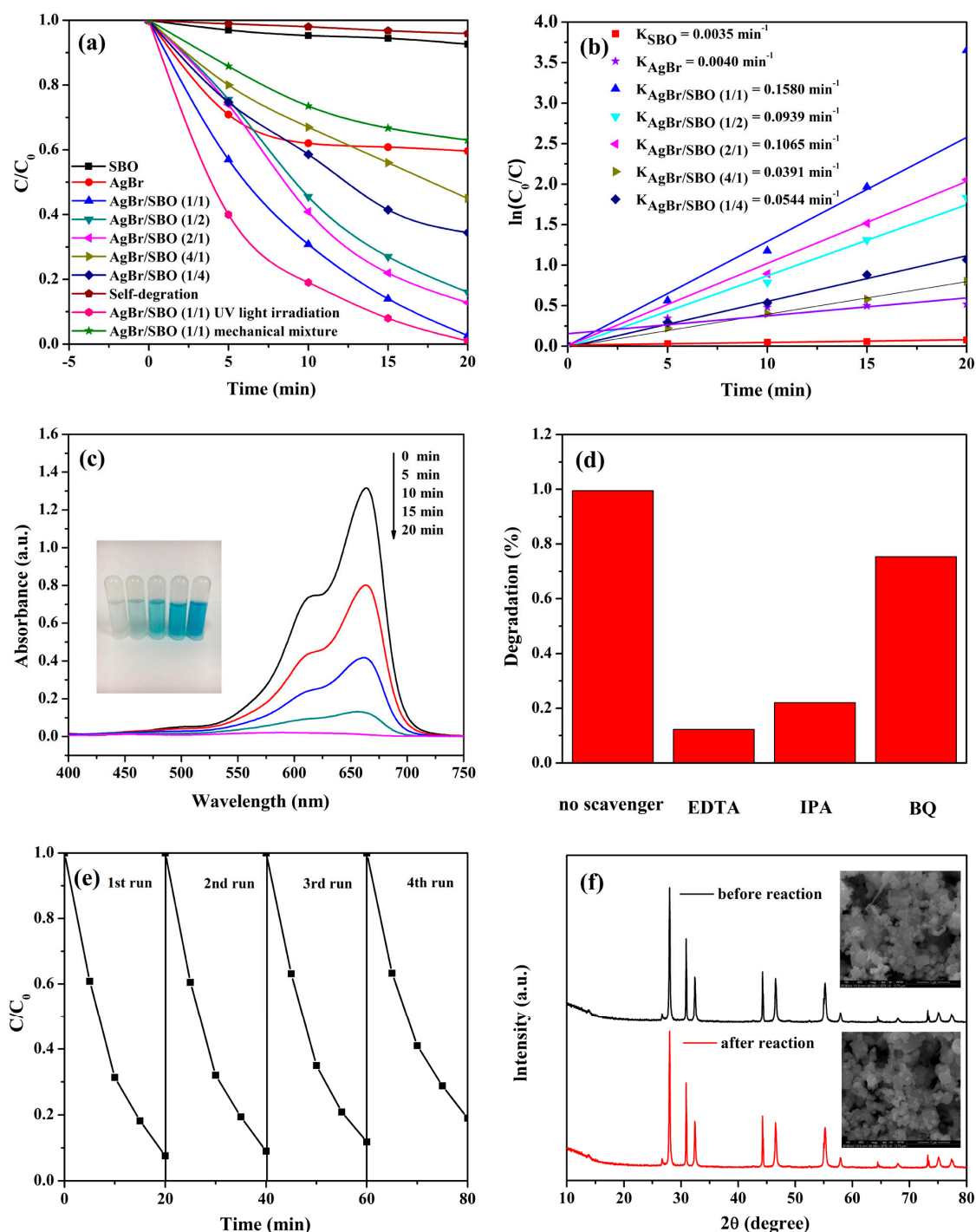**Figure 7.** (**a**) Photodegradation of MB solution without photocatalyst and over SBO, AgBr, and AgBr/SBO composites; (**b**) kinetic plot of the photodegradation of MB solution versus irradiation time; (**c**) absorption spectra of MB solution over AgBr/SBO (1/1) as a function of reaction time; (**d**) MB degradation efficiency on AgBr/SBO(1/1) adding some scavengers; (**e**) cycling experiments for the degradation of MB over AgBr/SBO (1/1); (**f**) XRD patterns of AgBr/SBO (1/1) together with SEM images shown in insets before and after degradation reaction.

The photostability of AgBr/SBO heterostructured catalyst is further investigated by performing the successive MB degradation experiments. Figure 7e shows that the as-synthesized AgBr/SBO (1/1) composite stands an excellent stability without obvious decay in photocatalytic performance after four recycles for the degradation of MB. As presented in Figure 7f, similar XRD patterns and SEM images before and after the degradation reaction further demonstrate that the AgBr/SBO heterostructured catalysts have high stability.

2.5. Photocatalytic Mechanism of AgBr/SBO Catalysts

The electrochemical impedance spectra (EIS) and transient photocurrent responses of pure AgBr, SBO and AgBr/SBO (1/1) composite are further measured to thoroughly comprehend the transfer and recombination of photoinduced charges in the as-synthesized photocatalysts. The EIS plots presented in Figure 8a clearly show that the semicircle of AgBr/SBO (1/1) is much smaller than that of pure SBO and AgBr, which shows the significant decrease of the charge transfer resistance in AgBr/SBO (1/1) composite due to the formation of a heterojunction [42]. The measured results clearly show a greatly reduced recombination rate of photoinduced charge carriers in AgBr/SBO (1/1) composite in comparison with pure AgBr and SBO. In addition, the photocurrent responses were further measured to further investigate the separation rate of photogeneraged electrons and holes in catalysts. Generally, photocatalysts with higher photocurrent density have a higher separation rate of photogenerated electron-hole pairs and possess more efficient catalytic performance [43]. It can be seen from Figure 8b that AgBr/SBO (1/1) heterostructured composite exhibits a remarkably enhanced transient photocurrent density in comparison with pure AgBr and SBO. This clearly confirms the intrinsic advantages of AgBr/SBO heterostructured composite in promoting the separation of photoinduced charges.
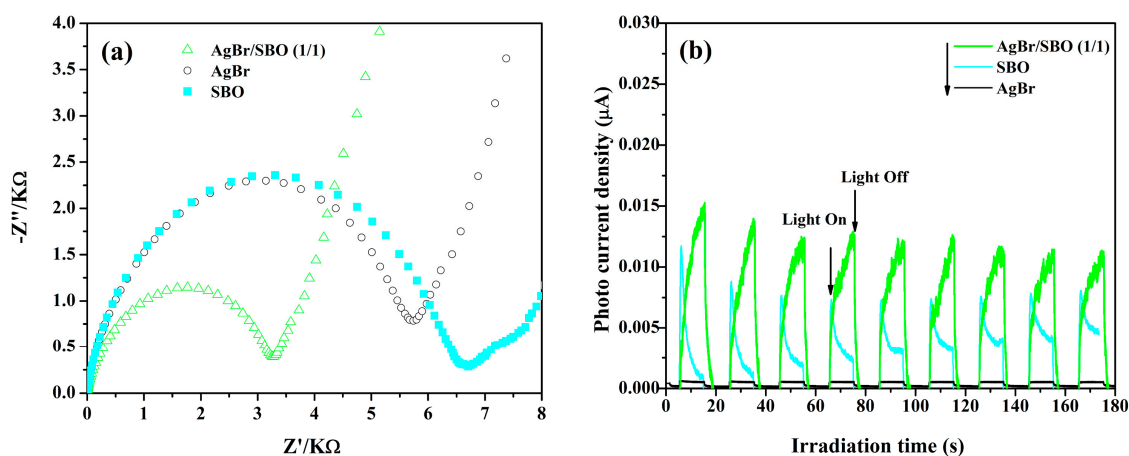

Figure 8. (**a**) EIS plots and (**b**) transient photocurrent curves of AgBr, SBO, and AgBr/SBO (1/1) catalysts.

The related mechanism for the photodegradation of MB solution over AgBr/SBO composites is illustrated in Figure 9. The relevant equations determining the band edge positions of SBO and AgBr are as below [44]:

$$E_{CB} = X - E_e - 0.5E_g \tag{2}$$

$$E_{VB} = E_{CB} + E_g \tag{3}$$

where E_{VB} and E_{CB} and are the valence band and conduction band and edge potentials, E_e is the energy of free electrons in a standard hydrogen electrode (4.5 eV), and X is the absolute electronegativity of a semiconductor. For AgBr and SBO, the values of X are 5.81 eV and 5.8 eV, respectively. The measured E_g of AgBr and SBO are 2.43 and 1.25 eV. Thus, the E_{CB} and E_{VB} of AgBr are calculated to be 0.09 and 2.52 eV, and the E_{CB} and E_{VB} of SBO are 0.68 and 1.93 eV, respectively. In the AgBr/SBO heterojunction, more photogenerated electrons and holes are excited under visible light irradiation

due to the narrow band gap. The photoinduced electrons from the CB of AgBr can easily transfer to the CB of SBO at the AgBr/SBO interface since the CB potential of SBO is less positive than that of AgBr. The photoinduced holes accumulating in the VB of AgBr can lead to efficient separation of photogenerated charges and hinder their recombination. The electrons transferring to the CB of SBO and AgBr are unable to generate $\bullet O_2^-$ from the dissolved O_2 by photoreduction because the CB edge potentials of SBO, AgBr (0.68 eV, 0.09 eV vs. NHE) does not reach the standard potential of $O_2/\bullet O_2^-$ (-0.33 eV vs. NHE) [45]. However, as presented in Figure 9, the CB edge potential of SBO is more negative than the reduction potential of O_2/H_2O_2 (0.695 eV vs. NHE), which can be enough to reduce O_2 to H_2O_2. Then the photogenerated H_2O_2 is reacted with e^- to produce $\bullet OH$ radicals, which leads to the direct oxidization of organic dyes. In addition, the photogenerated h^+ from the VB of AgBr are capable of oxidizing H_2O molecules into the $\bullet OH$ radicals, since the VB edge potential of AgBr (2.52 eV) is more positive than the standard potential of $\bullet OH/OH^-$ (1.99 eV vs. NHE) [46]. At the same time, the photoinduced holes and $\bullet OH$ radicals can also directly oxidize dye molecules owning to the photoinduced $\bullet OH$ radicals and holes with strong oxidation ability. As a result, $\bullet OH$ and h^+ are the major active species during the photodegradation process, which has been certified by the results from trapping experiments presented in Figure 7d. In general, the efficient photodegradation progress of MB solution over AgBr/SBO heterostructured catalysts can be described as the following equations:
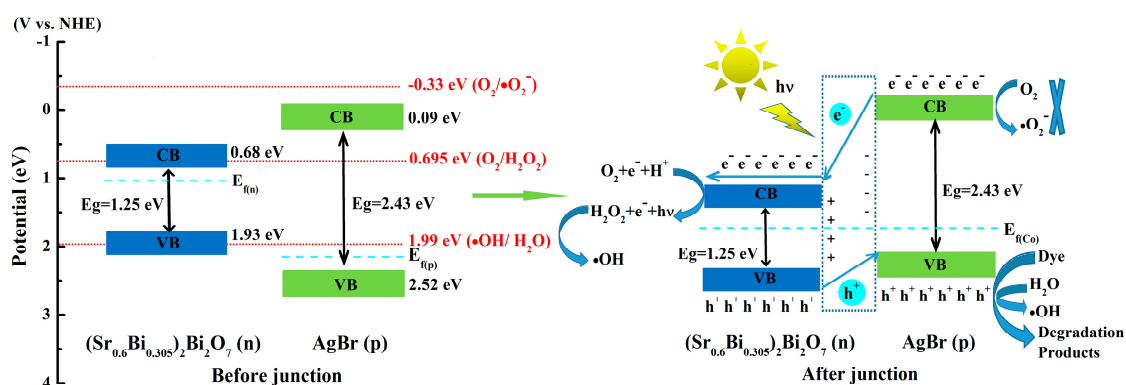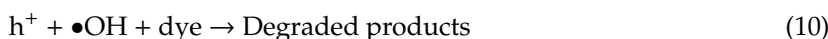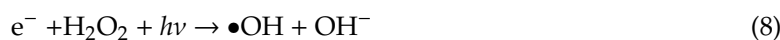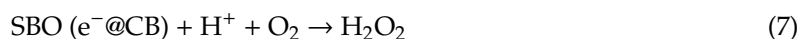
$$\text{SBO-AgBr (n-p)} + h\nu \text{ (visible)} \rightarrow \text{SBO-AgBr (n-p)} (h^+@VB + e^-@CB) \tag{4}$$

$$\text{AgBr } (e^-@CB) \rightarrow \text{SBO } (e^-@CB) \tag{5}$$

$$\text{SBO } (h^+@VB) \rightarrow \text{AgBr } (h^+@VB) \tag{6}$$

$$\text{SBO } (e^-@CB) + H^+ + O_2 \rightarrow H_2O_2 \tag{7}$$

$$e^- + H_2O_2 + h\nu \rightarrow \bullet OH + OH^- \tag{8}$$

$$\text{AgBr } (h^+@VB) + H_2O + OH^- \rightarrow \bullet OH \tag{9}$$

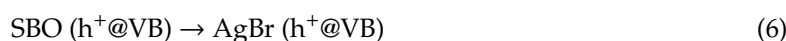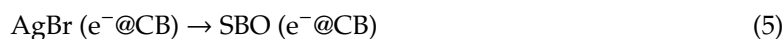$$h^+ + \bullet OH + \text{dye} \rightarrow \text{Degraded products} \tag{10}$$

Figure 9. Schematic diagram of the proposed mechanism for photoinduced charge carrier transfer over AgBr/SBO heterojunction under visible light irrdition.

3. Materials and Methods

3.1. Preparation of Photocatalysts

All chemicals for synthesis were analytical grade and used without extra purification. Pure SBO photocatalysts were prepared by using the hydrothermal method. The experimental procedure was as follows: 5 mmol of $NaBiO_3\cdot2H_2O$ and 10 mmol of $Sr(NO_3)_2$ were dispersed into 30 mL of distilled water to acquire solution A and B, respectively, accompanying by a about 10 min stirring. Then solution A

was poured in solution B and kept a 30 min stirring to form the brown-yellow and uniform suspensions. 4 M NaOH solution was used to tune up the pH value of mixed suspension accompanying by a 30 min continuous stirring. Subsequently, the as-formed suspension was moved into a 100 mL of Teflon lined hydrothermal autoclave and kept at 160 °C for 6 h. Then the resultant products were collected by centrifugation, washing with distilled water and absolute ethanol three times. Finally, the obtained samples were kept in the oven by drying at 60 °C for 12 h.

AgBr/SBO samples were prepared by using the chemical deposition precipitation method. The molar ratio of AgBr to SBO used in this work was 4/1, 2/1, 1/1, 1/2, and 1/4, respectively. During the process of synthesis, the equal mole of KBr and $AgNO_3$ (4 mmol, 2 mmol, 1 mmol, 0.5 mmol, and 0.25 mmol) were respectively dispersed in 30 mL of distilled water. 0.762 g of SBO powder was dissolved into the KBr solution by ultrasonic irradiation for 10 min. Then $AgNO_3$ aqueous solution was added dropwise into the above stirred SBO suspension. The composite was produced by filtration, washing three times with absolute alcohol and distilled water, and drying at 60 °C for 12 h after a 3 h stirring. In addition, pure AgBr was synthesized by the same procedure mentioned above without the presence of SBO.

3.2. Characterizations of Photocatalysts

The crystalline structures of the prepared products were characterized by a Bruker D8-Advance powder *X*-ray diffractometer (XRD) operating at 40 kV and room temperature with Cu-Kα radiation (λ = 0.1541 nm) in the 2θ range from 20° to 80°. A Quanta 450 FEG field emission scanning electron microscope (FESEM, FEI, Eindhoven, The Netherlands) and a FEI Tecnai G20 transmission electron microscopy (TEM, FEI, USA) were used to observe the morphologies of the resultant samples. The elemental compositions of as-prepared catalysts were determined using a Thermo Noran VANTAG-ESI energy dispersive X-ray spectroscopy (EDS, FEI, Eindhoven, The Netherlands). Fourier transform infrared spectra were recorded using a Nicolet 6700 spectrometer (FTIR, ThermoFisher Scientific Inc., Waltham, MA, USA) equipped with a KBr beamsplitter. The elemental compositions and chemical state of AgBr/SBO catalysts were measured by ESCALAB 250XI X-ray photoelectron spectrometer (XPS, Thermo Fisher Scientific Inc., Waltham, MA, USA). Ultraviolet-visible diffuse reflectance spectrum (UV-vis DRS) was measured on a UV-vis spectrometer (Puxi TU-1901, Beijing, China) using $BaSO_4$ as a reference material to characterize the optical property of catalysts.

3.3. Photocatalytic Performance Measurement

The photocatalytic performance of pure SBO, AgBr, and AgBr/BSO catalysts were measured by degrading MB under visible light illumination. A 300 W xenon lamp (PLS-SXE300C, Perfectlight Technology, Beijing, China) was used as the light source. Pure visible light source was acquired by a cutoff filter (λ > 420 nm). The typical process of photodegradation of MB was as follows: (i) 0.2 g of catalyst powder was added into a glass beaker containing 100 mL of MB aqueous solution with a concentration of 5 mg/L. (ii) The suspension was vigorously stirred for 30 min in darkness to guarantee the adsorption/desorption equilibrium between MB and photocatalyst. (iii) At a given time interval, the 4 mL of the suspension was taken out and centrifuged to filtrate the catalyst powders after the photoreaction and the supernatant was taken for analysis.

3.4. Photoelectrochemical Measurement

The electrochemical impedance spectra (EIS) of samples was measured on an electrochemical workstation (Vertex. C. EIS, brillante, Tianjin, China) in a standard three-electrode system. The Pt flake, Ag/AgCl, and as-synthesized sample were used as the counter electrode, reference electrode, and the working electrode, respectively. In all the electrochemical measurements, an aqueous solution containing 0.5 M KOH was used as the electrolyte. The sunlight was simulated by using a 300 W xenon lamp equipped with an AM 1.5G filter. The Nyquist plot was measured in the frequency range from

0.1 Hz to 100 kHz. The measurements on transient photocurrent response of samples were carried out using a Keysight B1500A semiconductor device analyzer (Agilent Technologies, Santa Clara, CA, USA).

4. Conclusions

The pyrochlore-type SBO was first investigated as a photocatalyst considering the fact that it not only possesses the particular crystal structure and but also contains Bi^{3+} and Bi^{5+} mixed valent states similar to another Bi-based oxide Bi_2O_4 with high photocatalytic degradation efficiency. AgBr/SBO composites were prepared by using the deposition precipitation method to further improve the photocatalytic performance of SBO. The samples were characterized by XRD, FTIR, XPS, FESEM, TEM, and UV-Vis DRS, respectively. The as-prepared AgBr/SBO composites showed a better photocatalytic performance than pure SBO and AgBr for the degradation of MB solution. In particular, AgBr/SBO (1/1) exhibited the best photocatalytic activity and completely degraded the MB solution after 20 min visible light irradiation. The trapping experiments showed that •OH and h^+ radicals are the major active species and considered to play a key role in the MB degradation process. The measurements on electrochemical impedance spectra and photocurrent responses further indicated that the significant improvement in the photocatalytic performance of AgBr/SBO composites is mainly attributed to the increase of light absorption and efficient separation of photoinduced charges due to the construction of a heterojunction between AgBr and SBO.

References

1. Kyung, H.; Lee, J.; Choi, W. Simultaneous and synergistic conversion of dyes and heavy metal ions in aqueous TiO_2 suspensions under visible-light illumination. *Environ. Sci. Technol.* **2005**, *39*, 2376–2382. [CrossRef] [PubMed]

2. Chen, C.; Ma, W.; Zhao, J. Semiconductor-mediated photodegradation of pollutants under visible-light irradiation. *Chem. Soc. Rev.* **2010**, *39*, 4206–4219. [CrossRef] [PubMed]

3. Kisch, H. Semiconductor photocatalysis mechanistic and synthetic aspects. *Angew. Chem. Int. Ed.* **2013**, *52*, 812–847.

4. Tong, H.; Ouyang, S.; Bi, Y.; Umezawa, N.; Oshikiri, M.; Ye, J. Nano-photocatalytic materials: Possibilities and challenges. *Adv. Mater.* **2012**, *24*, 229–251.

5. Wang, H.; Zhang, L.; Chen, Z.; Hu, J.; Li, S.; Wang, Z.; Wang, X. Semiconductor heterojunction photocatalysts: Design, construction, and photocatalytic performance. *Chem. Soc. Rev.* **2014**, *43*, 5234–5244. [CrossRef] [PubMed]

6. Lin, B.; Yang, G.; Yang, B.; Zhao, Y. Construction of novel three dimensionally ordered macroporous carbon nitride for highly efficient photocatalytic activity. *Appl. Catal. B Environ.* **2016**, *198*, 276–285. [CrossRef]

7. Fujishima, A.; Honda, K. Electrochemical photolysis of water at a semiconductor electrode. *Nature* **1972**, *238*, 37–38. [CrossRef] [PubMed]

8. Hernández-Alonso, M.D.; Fresno, F.; Suárez, S.; Coronado, J.M. Development of alternative photocatalysts to TiO_2: Challenges and opportunities. *Energy Environ. Sci.* **2009**, *2*, 1231–1257.

9. Kumar, S.G.; Devi, L.G. Review of modified TiO_2 photocatalysis under UV/Visible light: Selected results and related mechanisms on interfacial charge carrier transfer dynamics. *J. Phys. Chem. A* **2011**, *115*, 13211–13241. [CrossRef]

10. Tian, J.; Zhao, Z.; Kumar, A.; Boughton, R.I.; Liu, H. Recent progress in design, synthesis, and applications of one-dimensional TiO$_2$ nanostructured surface heterostructures: A review. *Chem. Soc. Rev.* **2014**, *43*, 6920–6937. [CrossRef]

11. Zhao, X.; Liu, H.; Qu, J. Photoelectrocatalytic degradation of organic contaminants at Bi$_2$O$_3$/TiO$_2$ nanotube array electrode. *Appl. Surf. Sci.* **2011**, *257*, 4621–4624. [CrossRef]

12. Fu, H.; Pan, C.; Yao, W.; Zhu, Y. Visible-light-induced degradation of rhodamine B by nanosized Bi$_2$WO$_6$. *J. Phys. Chem. B* **2005**, *109*, 22432–22439. [CrossRef]

13. Kudo, A.; Omori, K.; Kato, H. A novel aqueous process for preparation of crystal form-controlled and highly crystalline BiVO$_4$ powder from layered vanadates at room temperature and its photocatalytic and photophysical properties. *J. Am. Chem. Soc.* **1999**, *121*, 11459–11467. [CrossRef]

14. Zhang, K.; Liu, C.; Huang, F.; Zheng, C.; Wang, W. Study of the electronic structure and photocatalytic activity of the BiOCl photocatalyst. *Appl. Catal. B Environ.* **2006**, *68*, 125–129. [CrossRef]

15. Shang, M.; Wang, W.; Zhang, L. Preparation of BiOBr lamellar structure with high photocatalytic activity by CTAB as Br source and template. *J. Hazard. Mater.* **2009**, *167*, 803–809. [CrossRef] [PubMed]

16. Wu, J.; Huang, F.; Lü, X.; Chen, P.; Wan, D.; Xu, F. Improved visible-light photocatalysis of nano-Bi$_2$Sn$_2$O$_7$ with dispersed s-bands. *J. Mater. Chem.* **2011**, *21*, 3872–3876. [CrossRef]

17. Dong, F.; Ho, W.K.; Lee, S.C.; Wu, Z.B.; Fu, M.; Zou, S.C.; Huang, Y. Template-free fabrication and growth mechanism of uniform (BiO)$_2$CO$_3$ hierarchical hollow microspheres with outstanding photocatalytic activities under both UV and visible light irradiation. *J. Mater. Chem.* **2011**, *21*, 12428–12436. [CrossRef]

18. Kako, T.; Zou, Z.; Katagiri, M.; Ye, J. Decomposition of organic compounds over NaBiO$_3$ under visible Light irradiation. *Chem. Mater.* **2007**, *19*, 198–202. [CrossRef]

19. Takei, T.; Haramoto, R.; Dong, Q.; Kumada, N.; Yonesaki, Y.; Kinomura, N.; Mano, T.; Nishimoto, S.; Kameshima, Y.; Miyake, M. Photocatalytic activities of various pentavalent bismuthates under visible light irradiation. *J. Solid State Chem.* **2011**, *184*, 2017–2022. [CrossRef]

20. Wang, W.; Chen, X.; Liu, G.; Shen, Z.; Xia, D.; Wong, P.K.; Yu, J.C. Monoclinic dibismuth tetraoxide: A new visible-light-driven photocatalyst for environmental remediation. *Appl. Catal. B Environ.* **2015**, *176*, 444–453. [CrossRef]

21. Kumada, N.; Hosoda, M.; Kinomura, N. Preparation of alkaline earth bismuth pyrochlores containing Bi^{5+} by low temperature hydrothermal reaction. *J. Solid State Chem.* **1993**, *106*, 476–484. [CrossRef]

22. Wang, X.; Liu, L.; An, H.; Zhong, Y.; Wang, D.; Tang, C.; Hu, C. (Sr0.6Bi0.305)2Bi2O7 as a new visible-light-responsive photocatalyst: An experimental and theoretical study. 2019; submitted.

23. Qu, Y.; Duan, X. Progress, challenge and perspective of heterogeneous photocatalysts. *Chem. Soc. Rev.* **2013**, *42*, 2568–2580. [CrossRef] [PubMed]

24. Moniz, S.J.A.; Shevlin, S.A.; Martin, D.J.; Guo, Z.; Tang, J. Visible-light driven heterojunction photocatalysts for water splitting-a critical review. *Energy Environ. Sci.* **2015**, *8*, 731–759. [CrossRef]

25. Reinosa, J.J.; Álvarez Docio, C.M.; Zapata-Ramírez, V.; Fernández, J.F. Hierarchical nano ZnO-micro TiO$_2$ composites: High UV protection yield lowering photodegradation in sunscreens. *Ceram. Int.* **2018**, *44*, 2827–2834. [CrossRef]

26. Reinosa, J.J.; Leret, P.; Álvarez Docio, C.M.; del Campo, A.; Fernández, J.F. Enhancement of UV absorption behavior in ZnO-TiO$_2$ composites. *Boletín Soc. Esp. Ceram. Vid.* **2016**, *55*, 55–62. [CrossRef]

27. Cao, J.; Luo, B.; Lin, H.; Xu, B.; Chen, S. Visible light photocatalytic activity enhancement and mechanism of AgBr/Ag$_3$PO$_4$ hybrids for degradation of methyl orange. *J. Hazard. Mater.* **2012**, *217*, 107–115. [CrossRef]

28. Liang, K.; Zheng, J.; Lai, H.H.; Nicholls, R.J.; Xiao, T.; Jones, M.O.; Edwards, P.P. Unusual reactivity of visible-light-responsive AgBr–BiOBr heterojunction photocatalysts. *J. Catal.* **2012**, *293*, 116–125.

29. Wang, D.; Xue, G.; Zhen, Y.; Fu, F.; Li, D. Monodispersed Ag nanoparticles loaded on the surface of spherical Bi$_2$WO$_6$ nanoarchitectures with enhanced photocatalytic activities. *J. Mater. Chem.* **2012**, *22*, 4751–4758. [CrossRef]

30. Hu, C.; Zhuang, J.; Zhong, L.; Zhong, Y.; Wang, D.; Zhou, H. Significantly enhanced photocatalytic activity of visible light responsive AgBr/Bi$_2$Sn$_2$O$_7$ heterostructured composites. *Appl. Surf. Sci.* **2017**, *426*, 1173–1181. [CrossRef]

31. Zhong, L.; Hu, C.; Zhuang, J.; Zhong, Y.; Wang, D.; Zhou, H. AgBr/MgBi$_2$O$_6$ heterostructured composites with highly efficient visible-light-driven photocatalytic activity. *J. Phys. Chem. Solids* **2018**, *117*, 94–100. [CrossRef]

32. Tian, J.; Hao, P.; Wei, N.; Cui, H.; Liu, H. 3D Bi_2MoO_6 nanosheet/TiO_2 nanobelt heterostructure: Enhanced photocatalytic activities and photoelectochemistry performance. *ACS Catal.* **2015**, *5*, 4530–4536. [CrossRef]

33. Cai, H.; Cheng, L.; Xu, F.; Wang, H.; Xu, W.; Li, F. Fabrication of the heterojunction catalyst $BiVO_4$/P25 and its visible-light photocatalytic activities. *R. Soc. Open Sci.* **2018**, *5*, 180752. [CrossRef]

34. Ke, D.; Peng, T.; Ma, L. Effects of hydrothermal temperature on the microstructures of $BiVO_4$ and its photocatalytic O_2 evolution activity under visible light. *Inorg. Chem.* **2009**, *48*, 4685–4691. [CrossRef] [PubMed]

35. Zheng, Y.; Zhang, X.; Zhao, J.; Yang, P. Assembled fabrication of α-Fe_2O_3/BiOCl heterojunctions with enhanced photocatalytic performance. *Appl. Surf. Sci.* **2018**, *430*, 585–594. [CrossRef]

36. Xu, W.; Liu, Z.; Fang, J.; Zhou, G.; Hong, X.; Wu, S.; Zhu, X.; Chen, Y.; Cen, C. CTAB-assisted hydrothermal synthesis of $Bi_2Sn_2O_7$ photocatalyst and its highly efficient degradation of organic dye under visible-light irradiation. *Int. J. Photoenergy* **2013**, *7*, 14502–14510.

37. Xia, D.; Wang, W.; Yin, R.; Jiang, Z.; An, T.; Li, G.; Zhao, H.; Wong, P.K. Enhanced photocatalytic inactivation of Escherichia coli by a novel Z-scheme g-C_3N_4/m-Bi_2O_4 hybrid photocatalyst under visible light: The role of reactive oxygen species. *Appl. Catal. B Environ.* **2017**, *214*, 23–33. [CrossRef]

38. Sun, M.; Li, S.; Yan, T.; Ji, P.; Zhao, X.; Yuan, K.; Wei, D.; Du, B. Fabrication of heterostructured $Bi_2O_2CO_3$/Bi_2O_4 photocatalyst and efficient photodegradation of organic contaminants under visible-light. *J. Harzard. Mater.* **2017**, *333*, 169–178. [CrossRef]

39. Yu, L.; Zhang, X.; Li, G.; Cao, Y.; Shao, Y.; Li, D. Highly efficient $Bi_2O_2CO_3$/BiOCl photocatalyst based on heterojunction with enhanced dye-sensitization under visible light. *Appl. Catal. B Environ.* **2016**, *187*, 301–309. [CrossRef]

40. Akple, M.S.; Low, J.; Wageh, S.; Al-Ghamdi, A.A.; Yu, J.; Zhang, J. Enhanced visible light photocatalytic H_2-production of g-C_3N_4/WS_2 composite heterostructures. *Appl. Surf. Sci.* **2015**, *358*, 193–203. [CrossRef]

41. Lin, X.; Xing, J.; Wang, W. Photocatalytic activities of heterojunction semiconductors Bi_2O_3/$BaTiO_3$: A strategy for the design of efficient combined photocatalysts. *J. Phys. Chem. C* **2007**, *111*, 18288–18293. [CrossRef]

42. Zhang, S.W.; Li, J.X.; Zeng, M.Y.; Zhao, G.X.; Xu, J.Z.; Hu, W.P. In situ synthesis of water-soluble magnetic graphitic carbon nitride photocatalyst and its synergistic catalytic performance. *ACS Appl. Mater. Int.* **2013**, *5*, 12735–12743. [CrossRef] [PubMed]

43. Liu, Y.; Wang, R.; Yang, Z.; Du, H.; Jiang, Y.; Shen, C. Enhanced visible-light photocatalytic activity of Z-scheme graphitic carbon nitride/oxygen vacancy-rich zinc oxide hybrid photocatalysts. *Chin. J. Catal.* **2015**, *36*, 2135–2144. [CrossRef]

44. Lin, H.; Cao, J.; Luo, B.; Xu, B.; Chen, S. Synthesis of novel Z-scheme AgI/Ag/AgBr composite with enhanced visible light photocatalytic activity. *Catal. Commun.* **2012**, *21*, 91–95. [CrossRef]

45. Hua, X.; Zhou, K.; Chen, B. Graphene/TiO_2/ZSM-5 composites synthesized by mixture design were used for photocatalytic degradation of oxytetracycline under visible light: Mechanism and biotoxicity. *Appl. Surf. Sci.* **2016**, *362*, 329–334. [CrossRef]

46. Bai, X.; Wang, L.; Zhu, Y. Visible photocatalytic activity enhancement of $ZnWO_4$ by graphene hybridization. *ACS Catal.* **2012**, *2*, 2769–2778. [CrossRef]